

The KiHM-9: A Novel Self-deploying PicoSat Antenna Design for Reflectarray Antennas

Nathan Coleman, Mitchel Skinner, Collin Ynchausti, Spencer Magleby, Larry Howell
 Brigham Young University
 350 Engineering Building Provo, UT 84602; (801) 422-2625
 ncolema4@byu.edu

Akash Biswas
 Florida International University
 11200 SW 8th St, Miami, FL 33199; (305) 348-2000

ABSTRACT

Reflectarray antennas are popular on satellites for their ability to achieve similar performance to parabolic antennas in a more compact volume. This project shows how integrating novel technologies achieves the benefits of larger antennas while maintaining the advantages of small satellites. The objective of this research is to create a reflectarray antenna for a holographic metasurface that utilizes the volume surrounding a CubeSat when stowed, incorporates a novel pin-less hinge, includes a self-deploying and stabilizing joint, and is manufactured out of space-grade materials. By using hinges embedded with membranes and magnets, issues with lubrication and outgassing may be avoided, and the same motion and stability of pin-joints may be maintained with no external structure required. These technologies also result in a self-deploying and self-stabilizing design. The Radii Controlled Embedded Lamina (RadiCEL) hinge design was incorporated into the final model and allows the geometry of the hinge joint to be specifically tuned to control the stress in the hinge membrane while minimizing required hinge volume. Metal meshes were used as membrane joints, increasing the durability and robustness of the hinge. Feasibility of the RadiCEL joint is shown through fatigue testing of various materials at a range of hinge radii. The testing shows the viability of metal meshes, as well as other common membranes. Magnets were used in a MaLO configuration, which allowed for a smaller footprint in the antenna and required no external actuation or power source to deploy and stabilize the antenna. Various prototypes of the system were manufactured and are presented. Modeling and testing efforts presented create various opportunities to build on current research to improve mission capability by increasing antenna gain while eliminating peripherals required for antenna deployment.

INTRODUCTION

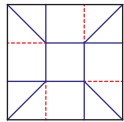
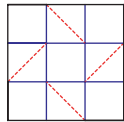
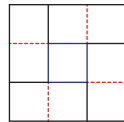
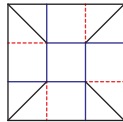
Trends in the aerospace industry have shown that the number of satellites launched into space each year has steadily increased for the last two decades.¹ One factor that has contributed to this trend is improved technology that has allowed for smaller satellites that are cheaper to launch. An example is the CubeSat, which first launched in 2003 and has since become a standard platform for simple space missions.²⁻⁵ CubeSats, along with other “PicoSats”, rely on antennas to establish radio transmission, as well as solar panels to power the satellite.⁶ Because the performance of antennas and solar panels is directly related to their surface area, engineers have turned to various methods, including origami, to in-

crease their ratio of deployed surface area to stowed volume.^{3,7}

High-gain antennas such as parabolic reflectors, phased arrays (PAs), electronically steered arrays (ESAs), reflectarrays (RAs), transmitarrays (TAs), and metasurface antennas (MAs) are commonly used in satellite communication systems and each has its own advantages and disadvantages. For example, PAs can dynamically steer their beams in a desired direction with a high level of beam agility.⁸ However, their designs are complex, and they require high power beam-forming mechanisms that increase both their cost and their profile. TAs and RAs are simple, cost-effective solutions that achieve high gains due to their large apertures, but they have

¹Notably, state-of-the-art reflectarrays with an aperture surface of $58\lambda^2$, designed to operate at 16 GHz for exhibiting the necessary realized gain of 26.4 dBi, place their feed antennas (e.g. horn antennas) at distance $H_f = 9.4\lambda$ (where, $\lambda = c/f$, f is the frequency of operation of the antenna and c is the speed of light) from the center of their apertures, that corresponds to

Table 1: Fold Pattern Candidates based on Patterns that can Fold around 1U CubeSats. The red dashed lines are valley folds, the blue solid lines are mountain folds, and the interior black solid lines are cuts. The selected pattern is highlighted.

Fold Pattern				
Fold Pattern Name	Origami Box with Corner Folds	Four-Sided Flasher	Kirigami 9-Panel	Kirigami 13-Panel
Number of Folds	16	16	8	12
Mountain Folds	12	12	4	8
Valley Folds	4	4	4	4
Number of Cuts	0	0	4	4
Number of Folds and Cuts	16	16	12	16
Rigid-Foldable	Yes	No	Yes	Yes
Special Thickness Accommodation	Yes	Yes	No	No

high-profile due to the feed source placed several wavelengths away from the reflective surface¹

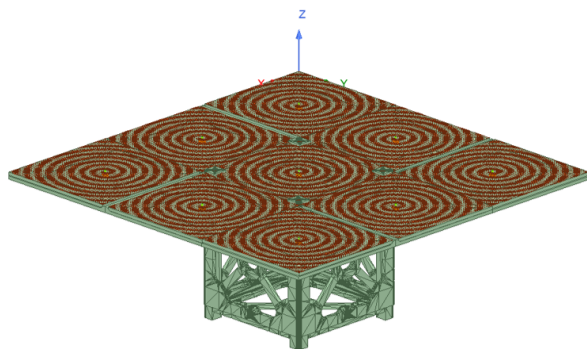


Figure 1: Initial deployed holographic metasurface antenna array concept design with 1U CubeSat structure.

Metasurface antennas, particularly holographic metasurface antennas (HMAs), have all the advantages of RAs and TAs, while, in addition, they are low-profile structures, making them promising candidates for use in satellite systems. Their performance is achieved using sub-wavelength unit cells (e.g., passive microstrip patch antennas of size $\lambda/5 \times \lambda/5$) properly distributed on their flat apertures, and fed by a single source placed at the center of the HMA's aperture. Despite the attractive electromagnetic properties of all these large aperture high-gain antennas, a big challenge is how to fold them for sending them into space. Folding antennas have an advantage when sending satellites to space; however, stowed antennas must be deployed, which often requires peripheral infrastructure. Reducing the mass

¹17.6cm.,⁹

of deployable antennas as well as reducing the mass of systems required to deploy the antennas is an important topic of research and focus of design.

Current satellites use a variety of methods to deploy and stabilize antennas, including telescoping booms,¹⁰⁻¹³ masts,¹⁴ exterior frames and trusses,¹⁵⁻¹⁷ stored strain energy in structures and tensioned cables,¹⁸⁻²⁴ pneumatics,^{25,26} and hard-stops.²⁷⁻³¹ These techniques are viable solutions for maintaining the desired performance of antennas; however, some of these techniques require external structures, which occupy payload volume and add mass. These mechanisms are also dependent on hinges and bearings, which can be subject to friction and wear.

The objective of this work was to create a holographic metasurface antenna (HMA) array that folds around the outside of a CubeSat and incorporates surrogate hinges, a stabilization technique, and deployment methods. The pattern for this antenna was developed with zero-thickness origami models, which were then modified to accommodate the thickness of each panel.

DESIGN

Design Objectives

The aim of this work was to create a foldable metasurface that uses surrogate hinges and other components appropriate for the space environment, can function reliably and repeatedly, deploys from a compact stowed area to a large deployed area, and is stable in a deployed configuration.

Pattern Selection

The deployed shape and aspect ratio requirement was for the deployed antenna to fill out a square 9-panel metasurface and to stow compactly on the outer sides of the CubeSat. An example is shown in Fig. 1, which shows how the unfolded holographic metasurface antenna would work with a 1U CubeSat structure.

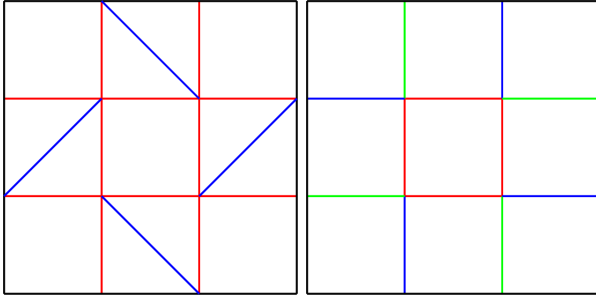


Figure 2: a) Analog flasher pattern with parameters $m=4$, $r=1$, $h=1$, and $dr=0$. Note that each repeating quadrant is referred to as a “gore”. b) Associated kirigami flasher pattern. Mountain folds are shown in red, valley folds are shown in blue, and cut lines are shown in green.

A kirigami flasher pattern was used for its simplicity and variety of folds. This pattern used a flasher pattern with the parameters $m = 4$, $r = 1$, $h = 1$, and $dr = 0$ ³²(shown in Fig. 2a), which was then modified to reduce the number of total panels and hinges by introducing cuts between gores, as shown in Fig. 2b. While modifying the design using kirigami principles introduces more degrees of the freedom to the flasher pattern, it was seen as desirable to reduce the complexity of integrating a pinless hinge design by reducing the number of folds in the pattern, as well as reducing the number of panels that were manufactured from 13 to 9. Note that each repeating section of a flasher pattern is referred to as a “gore”, and so each of the four repeating sections on this design will also be referred to as such.

Embedded Membrane Surrogate Hinges

When origami patterns are thickened to accommodate materials, the paper folds must be replaced with “surrogate hinges”. Often, this can be accomplished with a simple pin joint; however, this work sought to incorporate surrogate hinges which are appropriate for a space environment and which would not require lubrication. An embedded membrane hinge was chosen for its ability to leave deployed

panels on the same plane while maintaining a large usable surface area when deployed.

Embedded Membrane Hinge Geometry

The embedded membrane hinge design chosen was developed by Ynchausti et al.³³ This method uses two contacting circles of different radii to keep the membrane tensioned in both the open and closed positions, building off the Regionally Sandwiching of Compliant Sheets (ReCS) method of sandwiching a membrane between two panels. This modified approach increases control over the stress by varying the radius of the joint, allowing for less stress on the membrane while in a closed state, as shown in Fig. 3. When using this design, the larger radius, R_1 , is the limiting factor for the total thickness of the final panels, which in turn determines the mass and volume of the overall antenna. As such, R_1 was designed to be as small as possible, which was determined by the allowable stress in the membrane material. If the radius could be sufficiently thin, the limiting factor on the panel thickness would become the thickness required to achieve sufficient panel stiffness and limit compliance. The stress in the membrane hinge is given by

$$\sigma = \frac{Ec}{R} \quad (1)$$

which substituting $\sigma = \frac{Mc}{I}$ into Eqn.(1), when solved for the required radius becomes

$$R \geq \frac{Em}{2S_y} \quad (2)$$

where R is the radius of the bend, E is the modulus of elasticity of the membrane material, m is the thickness of the membrane, and S_y is the yield strength of the membrane.

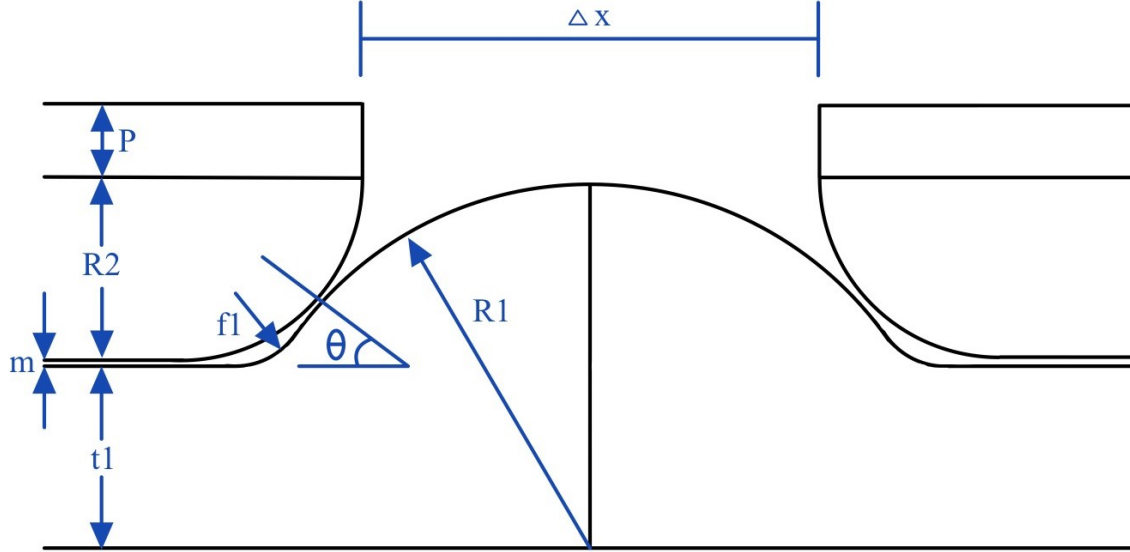


Figure 3: Geometry of hinge structure from Ynchausti et.al.³³ Note that the thickness of the reflectarray panels is given by P , which is added to R_2 to give $R_{2, effective}$.

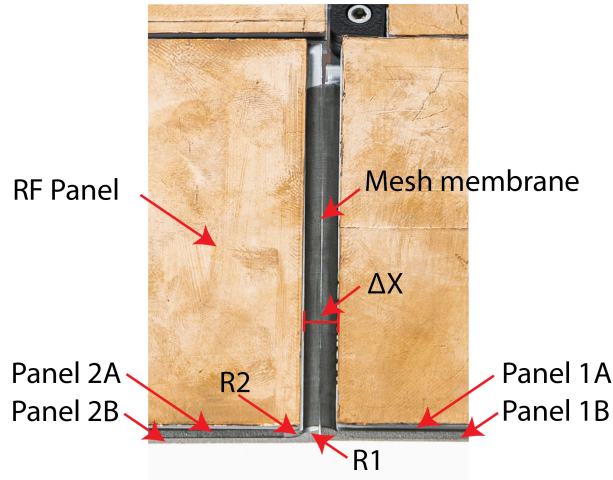


Figure 4: Close up of hinge design on final prototype.

A stainless steel mesh was chosen as the hinge membrane material for its ability to maintain performance in constant exposure to UV radiation. The mesh used is a 306 Stainless Steel 400 mesh which was woven in a non-crimped pattern with a hole diameter of $30 \mu\text{m}$ and a wire diameter of 0.03 mm . This mesh has a modulus of elasticity of $E = 193 \text{ GPa}$, a yield strength of $S_y = 290 \text{ MPa}$, and a thickness of $h = 0.08 \text{ mm}$. Note that in Fig. 3, the thickness of the PCB is added to R_2 to give $R_{2, effective}$. When treating the mesh as a solid membrane and substituting these parameters into Eqn. (2), the radius required to avoid yielding of the material is found to be

$$R \geq 2.66 \text{ cm.} \quad (3)$$

This is a relatively large radius considering the scale of the antenna and mesh. However, because of the nature of the mesh and how it is woven, if differed from a thin solid sheet which is assumed in the stress calculations. Here are a few factors that affect the stress of the stainless steel mesh:

1. The effective modulus of elasticity for a mesh of the same material would likely be different than that of a solid sheet.
2. Each wire in the mesh is not locked in place relative to the other wires around it, allowing it to more equally distribute loads within the mesh.
3. The total thickness of the mesh is greater than the thickness of any single wire being stressed, and so each wire can undergo more deflection before yielding than is predicted if it were the thickness of the mesh.
4. Due to the way the wires are woven over and under each other, the moment and stress applied to each wire are not equal to the moment applied to the mesh, and depend on the position of each wire in the weave. As such, Eqn. (2) is not a constant indicator of the actual maximum radius.
5. When one wire is stressed more than those around it, it can yield until the load is distributed to other wires, dispersing the load and

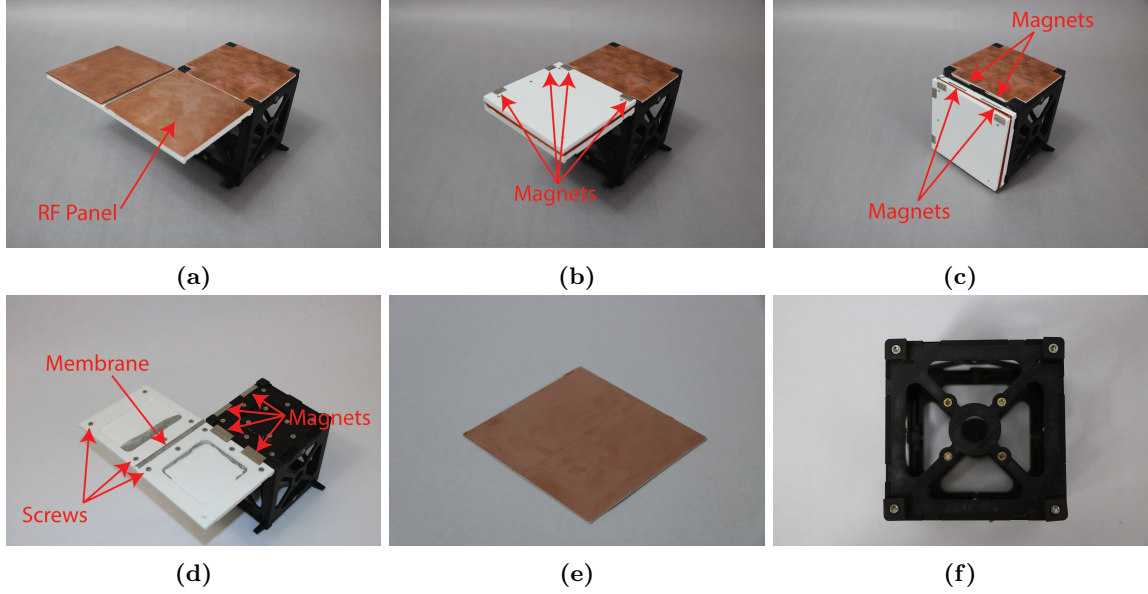


Figure 5: The initial prototype antenna, shown with one of four gores attached. a) Deployed antenna with mock RF panels attached. b) Half-closed antenna. The smaller magnets used for stabilization between panels are shown. c) Stowed antenna. The larger magnets used for stabilization between each gore to the CubeSat are shown. Note that all panels except for the central panel are covered and protected during stowage. d) Deployed antenna with RF panels removed to show screw attachment locations. Note the cutout in each the 1a and 2a (defined in Fig. 7) panels to reduce the mass of the overall antenna as well as to tension the mesh during assembly. e) Mock RF panel with the same thickness as the proposed reflectarray panels. d) CubeSat attachment points on the top of the CubeSat. Threads are made with brass inserts into the 3D printed CubeSat.

prolonging time to failure due to one weak link.

Eqn. (3) can be taken to be an upper limit for R . To account for these factors, a factor of 4 was used, resulting in a maximum radius of 0.5 cm, and this choice was verified through fatigue testing, detailed in Section . The geometry of the radius on each panel complicated the manufacturing process and could be optimized in future work for each hinge material chosen. From a maximum radius of 0.5 cm, values are found for each variable, as listed in Table 2.

From these design values and using equations presented in Ref.³³ for the relationship between radii (R_1 , R_2), the angle at which they are placed to each other (θ), and the total thickness (t_1), are calculated as

$$\theta = \frac{\pi}{2} \left(\frac{R_2}{R_1 + R_2} \right) \quad (4)$$

$$t_1 = (R_1 + R_2) \cos(\theta) - R_2 \quad (5)$$

Because the PCB panels are relatively thin, and

the membrane thickness is negligible, $R_{2, effective}$ becomes $R_2 + P$. This means that θ can be calculated as 40.39° and $t_1 = 0.3995 \text{ cm}$. With this design, the total surface area was 900 cm^2 , with the hinges taking up just 30 cm^2 , leaving 870 cm^2 or 96.6% of the total area available. Fig. 4 shows the hinge design with the calculated geometry from Table 2 in the final prototype.

Table 2: Geometric variables of designed hinge. Items with an asterisk were given, and not determined through calculation. Note that f_1 is only necessary to facilitate manufacturing of the internal corner at the bottom R_1 .

Variable	Description	Value
R_1	Radius of the bottom panel	0.5 cm
R_2	Radius of the top panel	0.25 cm
f_1^*	Fillet radius	0.2 cm
m^*	Membrane mesh thickness	0.008 cm
P^*	Thickness of reflectarray PCB	0.157 cm
$R_{2, Effective}$	Effective R2	0.407 cm

Deployment

The flasher pattern, upon which the kirigami pattern is based, has one degree of freedom; however, by adding cuts, seven additional degrees of freedom were introduced.

As the degrees of freedom increase, so does the complexity of incorporating a deployment mechanism. Therefore, to reduce this complexity, an internal deployment system was preferred. Because magnets were already used for stabilization, they appeared to be an ideal method to use for deployment as well; however, the effective range of the magnetic force was insufficient when compared to the travel required by the panels over the course of their deployment. As such, a lenticular fold is integrated in the frame of the CubeSat to act as a spring during deployment.

Lenticular Lock

The lenticular fold is a compliant mechanism that is manufactured in the shape of an Euler spiral, such that when deformed it stores strain energy and can lie flat. A deployable Euler spiral connector which was developed by Yellowhorse et al.³⁴ was integrated into each side of the CubeSat, as shown in Fig. 6. The lenticular fold is placed as far from the hinge as possible, to provide the largest moment arm to deploy the antenna panels. This functions such that the stowed state is an unstable state, and when a burn wire is cut the system will self-deploy. After 90° of motion the inner panels reach their hard stops, and the corner panels continue their motion due to their angular momentum.

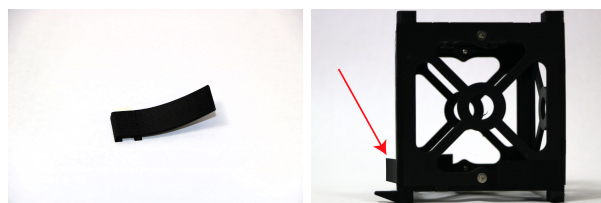


Figure 6: (Left) Lenticular fold which folds completely flat when stowed and provides a strong force. (Right) Side view of the lenticular fold showing its deployed position and displacement relative to a stowed flat position.

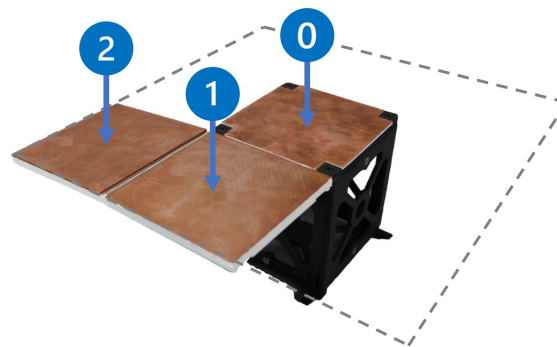


Figure 7: Numbering nomenclature of the panels during manufacturing. Note that “a” refers the top half of the panel (associated with R_2 on panels 1 and 2) and “b” refers to the bottom half of the panel (associated with R_1 on panels 1 and 2).

Stability

Magnets were selected for use in the stabilization method because of their ability to maintain a constant force over time without being subject to creep or stress relaxation.

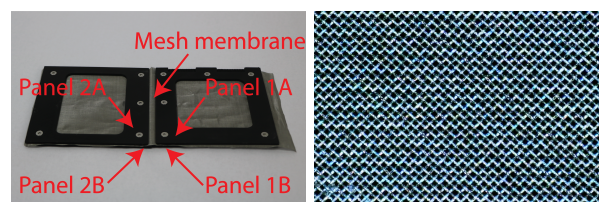


Figure 8: (Left) Panels used to tension and fatigue test the stainless steel mesh hinge. (Right) Close-up photograph from a microscope used to inspect the mesh for material wear and deformation, 50 zoom, after 100 open-close cycles.

Magnetic Embedded Hinges

In order to keep a low profile, magnets were used in the MaLO configuration developed by Pruet et al.³⁵ Integrating the MaLO design in the kirigami flasher gains additional stability as the magnets in each gore interlock with the magnets in the two adjacent gores. Although the magnets could be much smaller in practice, as the antenna would not be subject to a constant gravitational force while in orbit, this model sought to demonstrate the effectiveness of a magnetic embedded hinge in achieving stability by supporting the full mass of the panels in the

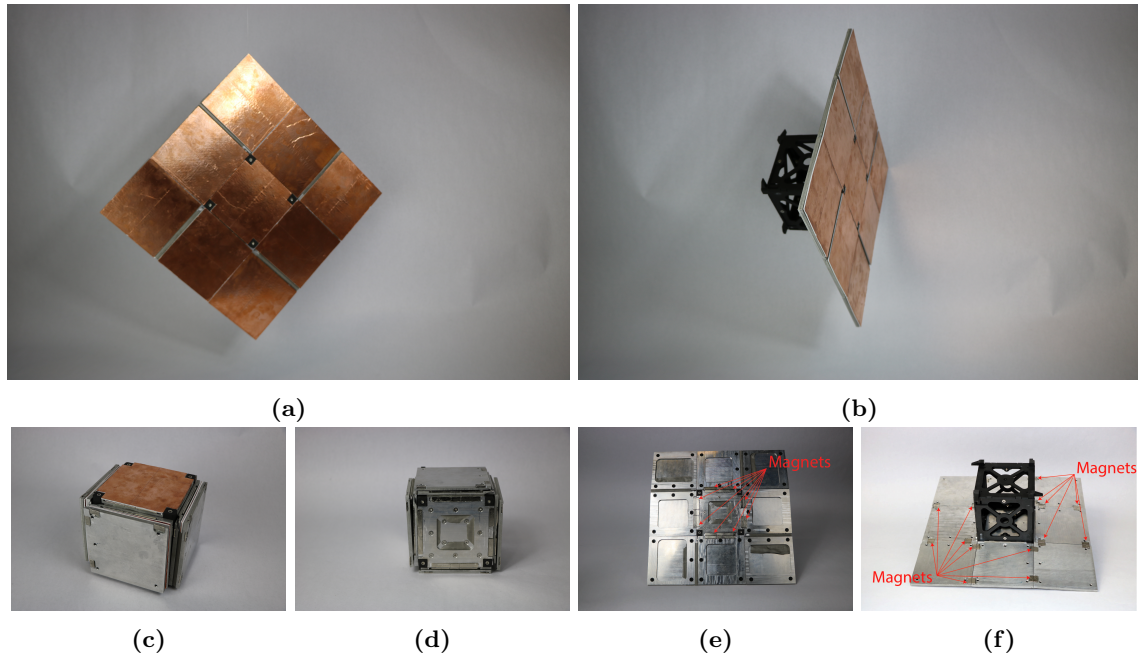


Figure 9: The final antenna prototype shown with all four gores attached. a) Antenna in deployed configuration, showing full pattern with 9 panels. Note the high area-use efficiency. b) Antenna in deployed configuration, side view. Note that in micro-gravity the antenna achieves remarkable flatness using the magnets for stabilization and panel thickness as hard stops. c) Stowed antenna. A burn wire would be used to delay deployment until desired, and that all panels besides the central panel are covered until deployed. d) The final antenna with mock RF panels removed, showing the top geometry holding the mesh in place and the magnet placement on the center panel. e) Final antenna with mock RF panels removed showing the geometry of each panel in the pattern. f) Bottom view of the final antenna showing magnet placement underneath each panel, which is used to interlock and stabilize each gore.

deployed state under Earth’s gravity. To verify that the force of the magnets would be sufficient to support the antenna panels, magnets were put into an Instron tensile testing machine. Two sizes of magnets were tested, with the larger magnets measuring 25.4 mm x 6.35 mm x 1.5875 mm, and the smaller magnets measuring 12.7 mm x 6.35 mm x 1.5875 mm. Over 10 tests, the average force of the larger magnets in a MaLO configuration was found to be 15.725 N. The same tests were run for the smaller magnets, resulting in an average force of 6.005 N, the standard deviation for both cases was 0.623 N. Magnet placement was designed to give a factor of safety for supporting the panels under earth’s gravity of 1.3.

PROTOTYPES AND TESTING

Fatigue Testing

To validate the hinge membrane selected, the mechanics and fatigue life were first validated using 3D printed panels, after which the final design was created and tested using materials similar to those that would be used in space.

As shown in Section , there are several unique factors that stem from using a woven mesh as the hinge membrane material as opposed to a uniform sheet material, each of which impact the calculated hinge radius needed to avoid yielding when bending, as given in Eqn. (2). Because of this, the calculated radius (Eqn. (3)) is taken to be an upper limit and not a design condition, and a smaller radius was chosen and validated using fatigue testing. A R_1 value of 0.5 cm and a R_2 value of 0.25 cm were chosen, as shown in Table 2.

To test this design, the stainless steel mesh was gripped between two panels and tensioned to 90 N

(20 lbf). The joint was then manually cycled 100 times. This testing set-up is shown in Fig. 8. The results of this can be seen in Fig. 8 b, which shows a 50 zoom of the mesh at the hinge location. Upon close inspection of the entire joint area, no mesh fibers were found to be broken, and no yielding of local wires could be found. By testing and creating better models for various membrane hinge materials, the radius of the hinge could be more accurately optimized for a given application, resulting in thinner and mass-reduced antennas.

Initial Prototype

A 3D printed model was created to verify design mechanics and behavior, as shown in Fig. 5. This model included surrogate reflectarray panels with the same thickness as actual panels to validate folding and stowage behaviors. This design also incorporated magnets to verify stabilization behavior.

Manufacturing of Final Prototype

The antenna was designed to be as simple as possible. The overall process used several manufacturing processes, including waterjet, CNC, and manual milling. Some challenges that had to be overcome were the thinness of each panel, the varying radii in each panel, and the differing hole placement requirements between different panels. These factors required the use of three separate vacuum table setups, as well as three separate fixture plates. The manufacturing process is shown in Appendix I, Table 3, and each part of the final design can be found in the Bill of Materials in Appendix I, Table 4.

RESULTS

Final Model

Following assembly, the antenna was placed in a micro-gravity simulation, as shown in Fig. 9b. The flatness indicates that the magnetic hinges and hard stops were successful in stabilizing the antenna in the desired position, and that the magnets used to interlock each gore to the next were effective in keeping each gore in the correct position relative to the gore next to it.

Epoxy was used to keep the magnets in place, and mechanical fasteners are recommended for future models. Additionally, the mesh hinges, which were held in place by the clamping force of the top and bottom panels, were noted to slip when left for extended periods of time, which would not be an issue in the zero-gravity environment of space,

but which is nonetheless an undesired behavior, and could be reduced by using epoxy in addition to the clamping force, to further secure the mesh within the panels. In future work, the antenna panels could also be made using forged carbon fiber, which may allow for easier manufacturing of the panel radii and production at scale.

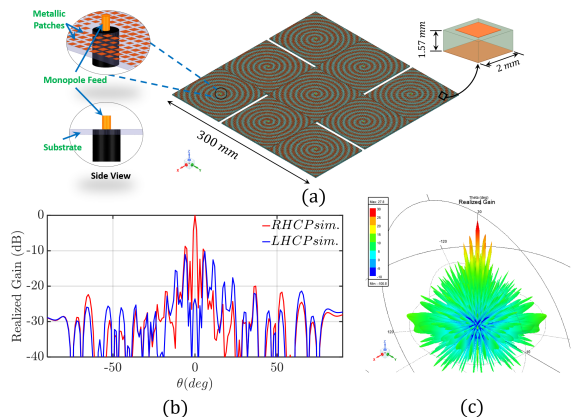


Figure 10: (a) A fully deployed 3×3 holographic metasurface antenna array; In the left inset, the monopole that feeds each panel is shown along with the coaxial cable used to power it up. In the right inset, a zoomed view of the 2mm sub-wavelength unit cell is shown consisting of a metallic square patch printed above a grounded substrate with a thickness of 1.57mm . (b) 2-D normalized radiation pattern, and (c) 3-D realized gain pattern of the HMA array.

RF Testing

To demonstrate the efficacy of the foldable holographic metasurface (HMA), its performance was evaluated through ANSYS HFSS simulations. Notably, aiming towards a circularly polarized broadside beam which is essential in satellite communications, a concentric circle-based holographic pattern was properly designed, as depicted in the right inset of Fig.10a. To feed the HMA, a monopole antenna was used, placed at the center of the radiating aperture and powered by a coaxial cable from the underside of the panel. Fig. 10a shows the final antenna design that consists of a 3×3 HMA array. Notably, the electric aperture of each HMA is $10\lambda \times 10\lambda$ designed to operate at 30GHz . Also, 4 rectangular cuts of size $\Delta x = 5.5\text{mm}$ were introduced in the HMA aperture accommodating the area of the hinges designed in Section (see Figs. 3 and 10). Fig. 10b shows the simulated normalized 2-D

radiation pattern and Fig. 10c the corresponding 3-D pattern of the entire 3×3 HMA array. As it is seen, a total realized gain of 27.8 dBi is achieved, which meets the nominal realized gain required to establish reliable communication between a terrestrial base station and a CubeSat.

CONCLUSION

The design and manufacturing of the KiHM-9 antenna demonstrates the effectiveness of origami as a starting point for pattern selection, embedded membrane hinges for actuation, and embedded magnets for stability. Several areas of profitable research for the future stemming from this work are optimizing the hinge radius by creating better stress and fatigue models for materials used in membrane hinges and exploring different manufacturing methods and materials for the radius hinge design. By following the methodology laid out in this work, designers can create self-deploying and self-stabilizing space-based reflectarray antennas.

ACKNOWLEDGEMENTS

This paper is based on work supported by the Air Force Office of Scientific Research grant FA9550-19-1-0290 through Florida International University.

Special thanks and acknowledgement are given to BYU Prototyping Lab assistants Camilla Cave and Ethan Hall, who machined the final antenna panels for this work.

REFERENCES

- [1] E. B. Salas, “Number of satellites launched by year 2019,” Mar 2022. [Online]. Available: <https://www.statista.com/statistics/896699/number-of-satellites-launched-by-year/>
- [2] A. Toorian, K. Diaz, and S. Lee, “The cubesat approach to space access,” pp. 1–14, 2008.
- [3] Y. Rahmat-Samii, V. Manohar, and J. M. Kovitz, “For satellites, think small, dream big: A review of recent antenna developments for cubesats.” *IEEE Antennas and Propagation Magazine*, vol. 59, no. 2, pp. 22–30, 2017.
- [4] A. H. Lokman, P. J. Soh, S. N. Azemi, H. Lago, S. K. Podilchak, S. Chalermwisutkul, M. F. Jamlos, A. A. Al-Hadi, P. Akkaraekthalin, and S. Gao, “A review of antennas for picosatellite applications,” *International Journal of Antennas and Propagation*, vol. 2017, 2017.
- [5] Z.-Q. Liu, H. Qiu, X. Li, and S.-L. Yang, “Review of large spacecraft deployable membrane antenna structures,” *Chinese Journal of Mechanical Engineering*, vol. 30, no. 6, pp. 1447–1459, 2017.
- [6] N. Chahat, R. E. Hodges, J. Sauder, M. Thomson, and Y. Rahmat-Samii, “The deep-space network telecommunication cubesat antenna: Using the deployable ka-band mesh reflector antenna.” *IEEE Antennas and Propagation Magazine*, vol. 59, no. 2, pp. 31–38, 2017.
- [7] A.-S. Kaddour, C. A. Velez, M. Hamza, N. C. Brown, C. Ynchausti, S. P. Magleby, L. L. Howell, and S. V. Georgakopoulos, “A foldable and reconfigurable monolithic reflectarray for space applications,” *IEEE Access*, vol. 8, pp. 219 355–219 366, 2020.
- [8] R. J. Mailloux, “Phased array antenna handbook, third edition,” *Artech House*, 2017.
- [9] A. J. Rubio, A.-S. Kaddour, C. Ynchausti, S. Magleby, L. L. Howell, and S. V. Georgakopoulos, “A foldable reflectarray on a hexagonal twist origami structure,” *IEEE Open Journal of Antennas and Propagation*, vol. 2, pp. 1108–1119, 2021.
- [10] M. E. McEachen, *Compact Telescoping Array: Advancement from Concept to Reality*. [Online]. Available: <https://arc.aiaa.org/doi/abs/10.2514/6.2018-1945>
- [11] C. Leclerc, L. L. Wilson, M. A. Bessa, and S. Pellegrino, *Characterization of Ultra-Thin Composite Triangular Rollable and Collapsible Booms*. [Online]. Available: <https://arc.aiaa.org/doi/abs/10.2514/6.2017-0172>
- [12] J. A. Firth and M. R. Pankow, “Advanced dual-pull mechanism for deployable spacecraft booms,” *Journal of Spacecraft and Rockets*, vol. 56, no. 2, pp. 569–576, 2019. [Online]. Available: <https://doi.org/10.2514/1.A34243>
- [13] J. Block, M. Straubel, and M. Wiedemann, “Ultralight deployable booms for solar sails and other large gossamer structures in space,” *Acta Astronautica*, vol. 68, no. 7, pp. 984–992, 2011. [Online]. Available: <https://www.sciencedirect.com/science/article/pii/S0094576510003437>
- [14] H. Guoa, R. Liu, Z. Deng, and J. Zhang, “Dynamic characteristic analysis of large space deployable articulated mast,” *Procedia Engineering*, vol. 16, pp. 716–722, 2011, international Workshop on Automobile, Power and Energy Engineering. [Online]. Available: <https://www.sciencedirect.com/science/article/pii/S1877705811026476>
- [15] G. Greschik, J. M. Mejia-Ariza, T. M. Murphey, and S. K. Jeon, “Error suppression via tension for flexible square antenna panels and panel arrays,” *AIAA Journal*, vol. 53, no. 3, pp. 513–531, 2015. [Online]. Available: <https://doi.org/10.2514/1.J052691>
- [16] A. Tamura, S. Inoue, D. Kawarabayashi, M. Yamazaki, and Y. Miyazaki, *Deployment Dynamics of Self-deployable Truss Structure Consisting of Bi-convex Booms*. [Online]. Available: <https://arc.aiaa.org/doi/abs/10.2514/6.2017-0175>
- [17] D. Webb, B. Hirsch, V. Bach, J. Sauder, S. Bradford, and M. Thomson, “Starshade mechanical architecture & technology effort,” 01 2016.
- [18] C. M. Chilan, D. R. Herber, Y. K. Nakka, S.-J. Chung, J. T. Allison, J. B. Aldrich, and O. S. Alvarez-Salazar, “Co-design of strain-actuated solar arrays for spacecraft precision pointing and jitter reduction,” *AIAA Journal*, vol. 55, no. 9, pp. 3180–3195, 2017. [Online]. Available: <https://doi.org/10.2514/1.J055748>
- [19] N. A. Pehrson, S. P. Smith, D. C. Ames, S. P. Magleby, and M. Arya, *Self-Deployable, Self-Stiffening, and Retractable Origami-Based Ar-*

- rays for Spacecraft*. [Online]. Available: <https://arc.aiaa.org/doi/abs/10.2514/6.2019-0484>
- [20] Z. Chu, Z. Deng, X. Qi, and B. Li, "Modeling and analysis of a large deployable antenna structure," *Acta Astronautica*, vol. 95, pp. 51–60, 2014. [Online]. Available: <https://www.sciencedirect.com/science/article/pii/S0094576513003858>
- [21] R. Crawford, J. Hedgepeth, and P. Preiswerk, *Spoked wheels to deploy large surfaces in space*. [Online]. Available: <https://arc.aiaa.org/doi/abs/10.2514/6.1974-1267>
- [22] X. Qi, H. Huang, B. Li, and Z. Deng, "A large ring deployable mechanism for space satellite antenna," *Aerospace Science and Technology*, vol. 58, pp. 498–510, 2016. [Online]. Available: <https://www.sciencedirect.com/science/article/pii/S127096381630671X>
- [23] S. Dong and X. Yuan, "Pretension process analysis of prestressed space grid structures," *Journal of Constructional Steel Research*, vol. 63, pp. 406–411, 03 2007.
- [24] M. Luo, R. Yan, Z. Wan, Y. Qin, J. Santoso, E. H. Skorina, and C. D. Onal, "Orisnake: Design, fabrication, and experimental analysis of a 3-d origami snake robot," *IEEE Robotics and Automation Letters*, vol. 3, no. 3, pp. 1993–1999, 2018.
- [25] T. Ranzani, S. Russo, F. Schwab, C. J. Walsh, and R. J. Wood, "Deployable stabilization mechanisms for endoscopic procedures," in *2017 IEEE International Conference on Robotics and Automation (ICRA)*, 2017, pp. 1125–1131.
- [26] S. Zirbel, S. Magleby, B. Trease, and L. Howell. NASA, May 2014. [Online]. Available: <http://www.esmats.eu/amspapers/pastpapers/pdfs/2014/zirbel.pdf>
- [27] J. R. Blandino, B. Ross, N. Woo, Z. Smith, and E. McNaul, *Simulating CubeSat Structure Deployment Dynamics*. [Online]. Available: <https://arc.aiaa.org/doi/abs/10.2514/6.2018-1677>
- [28] H. Fang, S. Li, and K. W. Wang, "Self-locking degree-4 vertex origami structures," *Proceedings of the Royal Society A: Mathematical, Physical and Engineering Sciences*, vol. 472, no. 2195, p. 20160682, 2016.
- [29] E. T. Filipov, T. Tachi, and G. H. Paulino, "Origami tubes assembled into stiff, yet reconfigurable structures and metamaterials," *Proceedings of the National Academy of Sciences*, vol. 112, no. 40, pp. 12 321–12 326, 2015. [Online]. Available: <https://www.pnas.org/doi/abs/10.1073/pnas.1509465112>
- [30] J. Gattas and Z. You, "Geometric assembly of rigid-foldable morphing sandwich structures," *Engineering Structures*, vol. 94, pp. 149–159, 2015. [Online]. Available: <https://www.sciencedirect.com/science/article/pii/S0141029615001558>
- [31] P. Shemanski and B. Trease, "Compact directional and frictional hinges for flat folding applications," 08 2018, p. V05BT07A064.
- [32] R. J. Lang, K. A. Tolman, E. B. Crampton, S. P. Magleby, and L. L. Howell, "A review of thickness-accommodation techniques in origami-inspired engineering," *Applied Mechanics Reviews*, vol. 70, no. 1, 2018.
- [33] C. Ynchausti, S. Shirley, S. P. Magleby, and L. L. Howell, "Adjustable, radii-controlled embedded lamina (RadiCEL) hinges for folding of thick origami-adapted systems," *Mechanism and Machine Theory*, 2023, in Review.
- [34] A. Yellowhorse and L. L. Howell, "Deployable lenticular stiffeners for origami-inspired mechanisms," *Mechanics Based Design of Structures and Machines*, vol. 46, no. 5, pp. 634–649, 2018.
- [35] H. Pruett, N. Coleman, and S. P. Magleby, "Preliminary concepts for magnetic actuation and stabilization of origami-based arrays," in *International Design Engineering Technical Conferences and Computers and Information in Engineering Conference*. American Society of Mechanical Engineers (in review).

APPENDIX I

Table 3: Manufacturing Steps.

Step	Part	Operation	Manufacturing Method
1	All panels	Cut out profile	Waterjet
2	Vacuum plate	Mill	CNC
3	All fixture plates	Mill	CNC
4	All panels, top side	Mill	CNC with vacuum plate
5	All panels, bottom side	Mill	CNC with fixture plate
6	Stainless steel mesh	Cut	Scissors
7	Magnet	Attach	Epoxy
8	All gores	Connect panels	Screw together
9	All gores	Connect to central panel	Screw together
10	Antenna	Connect to CubeSat	Screw together

Table 4: Bill of Materials. See Fig. 7 for nomenclature on panel numbering.

Part	Quantity	Attachment Method
Panel 0A	1	Screws
Panel 0B	1	Screws
Panel 1A	4	Screws
Panel 1B	4	Screws
Panel 2A	4	Screws
Panel 2B	4	Screws
1" by 1/4" by 1/16" Neodymium Magnet	8	Epoxy
1/2" by 1/4" by 1/16" Neodymium Magnet	32	Epoxy
M3x5mm Flat Head Machine Screws	4	N/A
M4x5mm Flat Head Machine Screws	52	N/A
316 Stainless Steel 400 Mesh	1	Friction